

Comparison of optical potential for nucleons and Δ resonances

In electron scattering from nuclear targets

Arie Bodek and Tejin Cai

Department of Physics and Astronomy, University of Rochester, Rochester, NY 14627-0171

arXiv:2004.00087 Version 5 July 4, 2020 to be published in EPJC

Abstract. Precise modeling of neutrino interactions on nuclear targets is essential for neutrino oscillations experiments. The modeling of the energy of final state particles in quasielastic (QE) scattering and resonance production on bound nucleons requires knowledge of both the removal energy of the initial state bound nucleon as well as the average Coulomb and nuclear optical potentials for final state leptons and hadrons. We extract the average values of the real part of the nuclear optical potential for final state nucleons (U_{opt}^{QE}) as a function of the nucleon kinetic energy from inclusive electron scattering data on nuclear targets ($^{12}_6\text{C} + ^{16}_8\text{O}$, $^{40}_{20}\text{Ca} + ^{40}_{18}\text{Ar}$, ^6_3Li , $^{27}_{18}\text{Al}$, $^{56}_{26}\text{Fe}$, $^{208}_{82}\text{Pb}$) in the QE region and compare to calculations. We also extract values of the average of the real part of the nuclear optical potential for a $\Delta(1232)$ resonance in the final state (U_{opt}^Δ) within the impulse approximation. We find that U_{opt}^Δ is more negative than U_{opt}^{QE} with $U_{opt}^\Delta \approx 1.5 U_{opt}^{QE}$ for $^{12}_6\text{C}$.

PACS. 13.15.+g Neutrino interactions – 13.60.-r Photon and charged-lepton interactions with hadrons – 25.30.-c Lepton induced reactions

1 Introduction

Precise modeling of neutrino interactions on nuclear targets is essential for neutrino oscillations experiments [1–5]. The modeling of the energy of final state particles in quasielastic (QE) scattering and resonance production on bound nucleons requires knowledge of both the removal energy of the initial state bound nucleon as well as the average Coulomb and nuclear optical potentials for final state leptons and hadrons. In this communication we compare the values of the average nuclear optical potential for final state nucleons (U_{opt}^{QE}) as a function of the nucleon kinetic energy extracted from inclusive electron scattering data on nuclear targets in the QE region to calculations based on proton scattering data (on nuclear targets). In addition, we compare to values of the average nuclear optical potential for a $\Delta(1232)$ resonance in the final state (U_{opt}^Δ) extracted from a subset of the inclusive electron scattering data.

First we summarize some of the results of our previous publication [6] on removal energies and the average nuclear optical potential for final state nucleons extracted from inclusive quasielastic (QE) electron scattering data on a variety of nuclei. The analysis was done within the framework of the impulse approximation.

The diagrams on the top two panels of Fig. 1 illustrate electron QE scattering from an off-shell bound proton (left) and neutron (right). The diagrams on the bot-

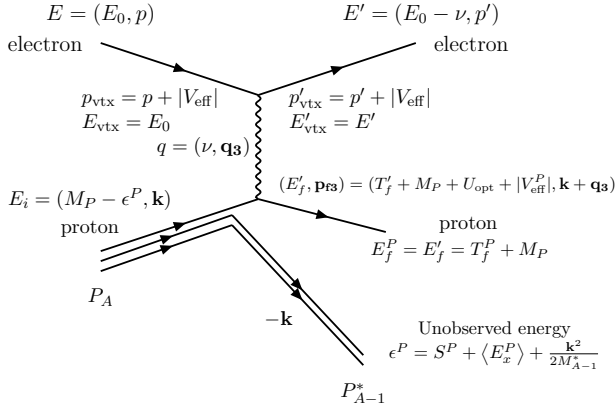
tom two panels show antineutrino ($\bar{\nu}$) QE scattering from an off-shell bound proton producing a final state neutron (left), and neutrino (ν) scattering from an off shell bound neutron producing a final state proton (right). The electron scatters from an off-shell nucleon of momentum $\mathbf{p}_i = \mathbf{k}$ bound in a nucleus of mass A . For electrons of incident energy E_0 and final state energy E' , the energy transfer to the target is $\nu = E_0 - E'$. The square of the 4-momentum transfer (Q^2), and 3-momentum transfer (\mathbf{q}_3) to a nucleon bound in the nucleus are:

$$Q^2 = 4(E_0 + |V_{eff}|)(E_0 - \nu + |V_{eff}|) \sin^2 \frac{\theta}{2} \quad (1)$$

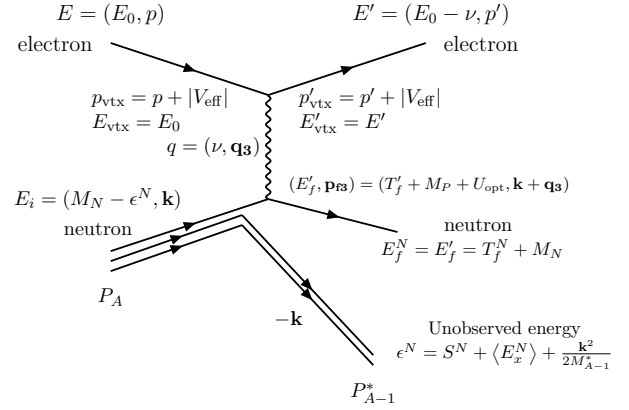
$$\mathbf{q}_3^2 = Q^2 + \nu^2.$$

We include the effects of the interaction of initial and final state electrons with the Coulomb field of the nucleus by using published values of the average Coulomb energy at the interaction vertex V_{eff} extracted from a comparison of electron and positron inclusive QE differential cross sections [7]. These values are in agreement with calculations based on charge distributions of nuclei [8]. In the diagrams of Fig. 1, the energies shown include both kinetic and potential energies. For electron scattering from bound protons, V_{eff} at the interaction vertex for a final state proton (in QE scattering), final state Δ^+1232 (in resonance production), and final state of mass W^+ (in

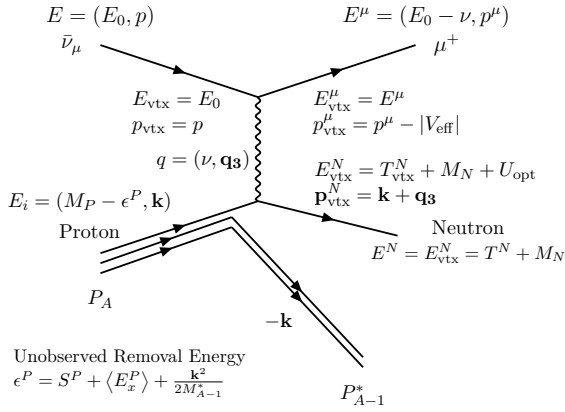
Electron scattering on proton



Electron scattering on neutron



Antineutrino Scattering on Proton



Neutrino Scattering on Neutron

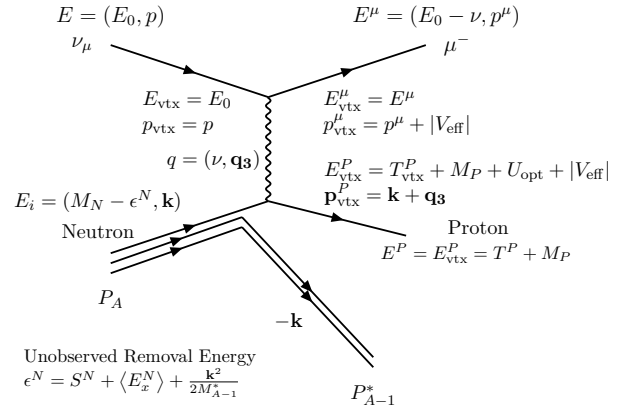


Fig. 1. The diagrams on the top two panels show electron QE scattering from an off-shell bound proton (left) and neutron (right). The diagrams on the bottom two panels show $\bar{\nu}$ QE scattering from an off-shell bound proton producing a final state neutron (left), and ν scattering from an off shell bound neutron producing a final state proton (right).

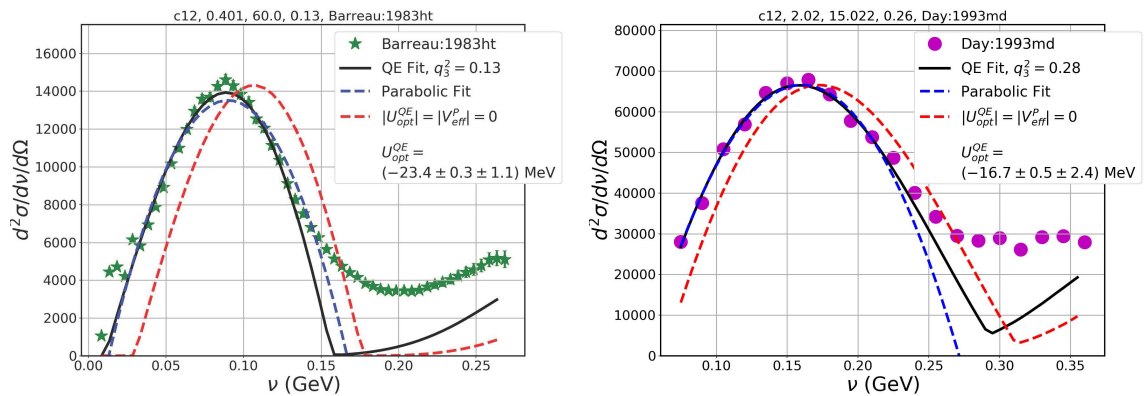


Fig. 2. Examples of fits for two out of 33 ^{12}C QE differential cross sections. The solid black curves are the RFG fits with the best value of U_{opt}^{QE} for the final state nucleon. The blue dashed curves are simple parabolic fits used to estimate the systematic error. The difference between $\nu_{peak}^{parabola}$ and ν_{peak}^{RFG} is used as a systematic error in our extraction of U_{opt}^{QE} . The first error shown in the legend is the statistical error in the fit. The second error is the systematic uncertainty which is much larger. The red dashed curve is the RFG model with $U_{opt}^{QE} = 0$ and $|V_{eff}^P| = 0$.

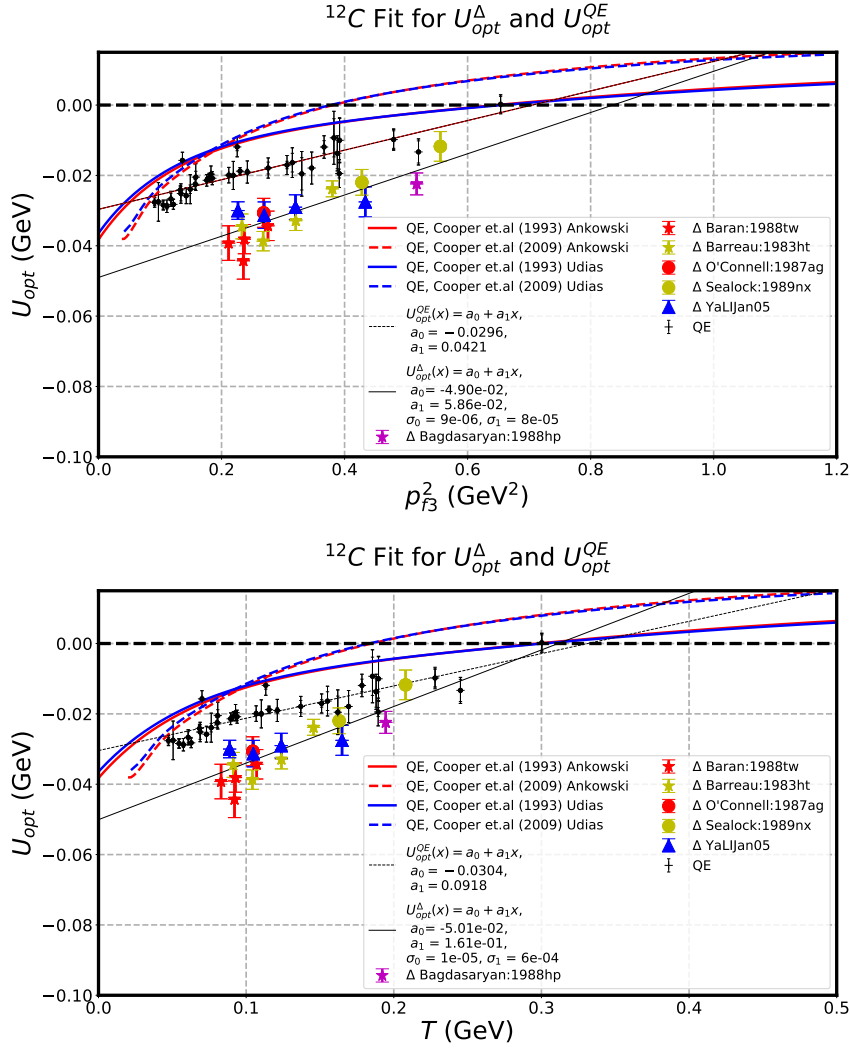


Fig. 3. Extracted values of U_{opt}^{QE} for the final state nucleon in QE scattering (small black markers) for 33 ^{12}C and four ^{16}O inclusive electron scattering spectra. Also shown are prediction for U_{opt}^{QE} calculated by and Jose Manuel Udias [39] and Artur. M. Ankowski [40] using the theoretical formalisms of Cooper 1993 [37] and Cooper 2009 [38]. The dashed grey lines are linear fits to the QE data. The larger markers are the values of U_{opt}^Δ for the final state $\Delta(1232)$ extracted from a subset of the data (15 ^{12}C spectra) for which the measurements extend to higher invariant mass. Here, the solid grey lines are linear fits to the U_{opt}^Δ values. The top and bottom panels show the measurements versus $p_{f3}^2 = (\mathbf{k} + \mathbf{q}_3)^2$, and versus hadron kinetic energy T , respectively.

inelastic scattering) are defined below.

$$|V_{eff}^P| = |V_{eff}^{\Delta+}| = |V_{eff}^{W+}| = \frac{Z-1}{Z} |V_{eff}|$$

For electron scattering from a neutron target we set $|V_{eff}^N| = 0$. The values of $|V_{eff}|$ that we use for various nuclei are given in Table 1.

2 Removal energy of initial state nucleons in a nucleus

In our analysis we use the impulse approximation. The nucleon is moving in the mean field (MF) of all the other

nucleons in the nucleus. The on-shell recoil excited $[A-1]^*$ spectator nucleus has a momentum $\mathbf{p}_{(A-1)^*} = -\mathbf{k}$ and a mean excitation energy $\langle E_x^{P,N} \rangle$. The off-shell energy of the interacting nucleon is

$$E_i = M_A - \sqrt{(M_{A-1}^*)^2 + \mathbf{k}^2} \quad (2)$$

$$= M_A - \sqrt{(M_{A-1} + E_x^{P,N})^2 + \mathbf{k}^2}$$

$$= M_{P,N} - \epsilon^{P,N}$$

$$\epsilon^{P,N} = S^{P,N} + \langle E_x^{P,N} \rangle + \frac{\mathbf{k}^2}{2M_{A-1}^*}.$$

Here, $M_P = 0.938272$ GeV is the mass of the proton, $M_N = 0.939565$ GeV is the mass of the neutron, and $S^{P,N}$ the

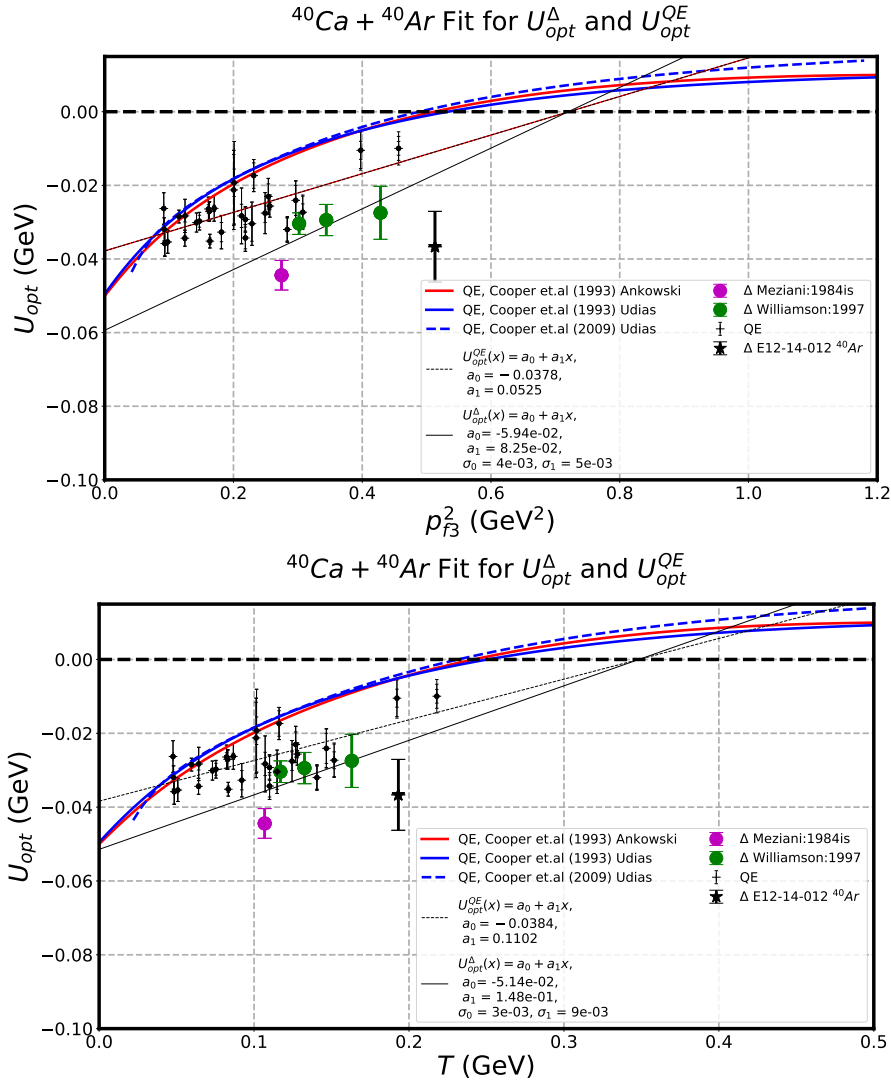


Fig. 4. Same as Fig. 3 for $^{40}\text{Ca} + ^{40}\text{Ar}$. The top and bottom panels show the measurements versus $p_{f3}^2 = (\mathbf{k} + \mathbf{q}_3)^2$, and versus hadron kinetic energy T , respectively.

separation energy (obtained from mass differences of the initial and final state nuclei) needed to separate the nucleon from the nucleus. In Ref. [6] we extract the mean excitation energy $\langle E_x^{P,N} \rangle$ (or equivalently the removal energy $\epsilon^{P,N}$) using spectral functions measured in exclusive electron scattering experiments on nuclear targets in which both the final state electron and proton are detected ($ee'P$). Some of the neutrino MC generators (e.g. current version of GENIE [9]) do not include the effect of the excitation of the spectator nucleus, nor do they include the effects of the interaction of the final state nucleons and hadrons with the Coulomb [7] and nuclear optical potentials of the nucleus.

3 Average nuclear optical potential for final state nucleons in QE scattering

We model the effect of the interaction of final state nucleons with the real part of the nuclear optical potential with a parameter $U_{opt}^{QE}(p_{f3}^2)$, where p_{f3}^2 is the square of the 3-momentum of the final state nucleon at the vertex. Alternatively, we also extract $U_{opt}^{QE}(T)$ where T is the kinetic energy of the final state nucleon. In the analysis we make the assumption that U_{opt}^{QE} for the proton and neutron are the same. The parameter $U_{opt}^{QE}(T)$ takes into account on average the effect of the real part of the nuclear optical potential and results in a modification of the energies of both the final state lepton and the final state nucleon.

The imaginary part of the optical potential results in interactions of the final state nucleon with nucleons in the spectator nucleus. These interactions can result in the knockout of additional nucleons as well as pion production. The effect of the imaginary part of the nuclear optical

potential (sometimes referred to as Final State Interaction - FSI) is included in current Monte Carlo generators using different models, including cascade models based on measured nucleon-nucleus scattering data. In this communication we only address the effects of the real part of the nuclear optical potential which modifies the energies of the final state lepton and nucleon. Note that when we refer to the *optical potential*, it is a shorthand for the *real part of the optical potential*. The energy of the final state nucleon in QE electron scattering is given by the following expressions:

$$\begin{aligned} \nu + (M_{P,N} - \epsilon^{P,N}) &= E_f^{P,N} \\ \mathbf{p}_{f3} &= (\mathbf{k} + \mathbf{q}_3) \\ E_f^{P,N} &= \sqrt{\mathbf{p}_{f3}^2 + M_{P,N}^2} + U_{opt}^{QE}(\mathbf{p}_{f3}^2) + |V_{eff}^{P,N}|. \\ T^{P,N} &= E_f^{P,N} - M_{P,N}, \end{aligned} \quad (3)$$

where $T^{P,N}$ is in the kinetic energy of the nucleon of mass $M_{P,N}$ after it leaves the nucleus and is in the same direction as \mathbf{p}_{f3} . We extract $U_{opt}^{QE}(\mathbf{p}_{f3}^2)$ and $U_{opt}^{QE}(T)$ from a comparison of the relativistic Fermi gas (RFG) model to measurements of inclusive QE e-A differential cross sections compiled in references [12] and [13]. The data samples (see references [14]- [34]) include the following elements which are of interest to current neutrino experiments: 33 $^{12}_6\text{C}$ spectra, five $^{16}_8\text{O}$ spectra, 29 $^{40}_{20}\text{Ca}$ spectra, and two $^{40}_{18}\text{Ar}$ spectra.

In addition, the data sample include four ^6_3Li spectra, eight $^{27}_{18}\text{Al}$ spectra, 30 $^{56}_{26}\text{Fe}$ spectra, and 23 $^{208}_{82}\text{Pb}$ spectra. Most (but not all) of the QE differential cross sections are available on the QE electron scattering archive [12,13].

In the extraction of the average nuclear optical potential for final state nucleons in QE scattering we only fit to the data in the top 1/3 of the QE distribution and extract the best value of $U_{opt}^{QE}(\mathbf{p}_{f3}^2)$ and $U_{opt}^{QE}(T)$. Here \mathbf{p}_{f3} is evaluated at the peak of the QE distribution. In the fit we let the normalization of the QE cross section float to agree with data. Figure 2 shows examples of two of the 33 fits to QE differential cross sections for $^{12}_6\text{C}$. The solid black curves are the RFG fits with the best value of U_{opt}^{QE} for the final state nucleon. The blue dashed curves are simple parabolic fits used to estimate the systematic error. The difference between $\nu_{peak}^{parabola}$ and ν_{peak}^{rfg} is used as a systematic error in our extraction of U_{opt}^{QE} . The first error shown in the legend of Figure 2 is the statistical error in the fit. The second error is the systematic uncertainty, which is much larger. The red dashed curve is the RFG model with $U_{opt}^{QE} = 0$ and $|V_{eff}^P| = 0$.

The extracted values of $U_{opt}^{QE}(\mathbf{p}_{f3}^2)$ versus \mathbf{p}_{f3}^2 from 33 $^{12}_6\text{C}$ QE spectra and five $^{16}_8\text{O}$ QE spectra are shown in the top panel of Figure 3. The same values as a function of the nucleon kinetic energy T are shown on the bottom panel. The extracted values of $U_{opt}^{QE}(\mathbf{p}_{f3}^2)$ versus \mathbf{p}_{f3}^2 (and T) from 29 $^{40}_{20}\text{Ca}$ QE spectra and two $^{40}_{18}\text{Ar}$ QE spectra are shown in Fig. 4.

Note that the figures also show values of the average optical potential for the Δ resonance which is discussed in a later section of this paper.

Similarly, values extracted for four ^6_3Li QE spectra, eight $^{27}_{18}\text{Al}$ QE spectra, 30 $^{56}_{26}\text{Fe}$ QE spectra and 23 $^{208}_{82}\text{Pb}$ QE spectra are shown in Fig.5.

We fit the extracted values of $U_{opt}^{QE}(\mathbf{p}_{f3}^2)$ versus \mathbf{p}_{f3}^2 for $\mathbf{p}_{f3}^2 > 0.1 \text{ GeV}^2$ to linear functions which are shown as dashed grey lines in Figures 3-5. We also show linear fits to U_{opt}^{QE} as a function of final state kinetic energy T. The intercepts at $\mathbf{p}_{f3}^2 = 0$ and the slopes of the fits to U_{opt}^{QE} versus \mathbf{p}_{f3}^2 , and the intercepts and slopes of the fits to U_{opt}^{QE} as a function of T are given in Table 1. Fits for $^{12}_6\text{C}$ using a different functional form are given in Table 2 of the Appendix.

Note that parameters for the average optical potential for the Δ resonance (discussed in a later section of this paper) are also included in Tables 1 and in Table 2.

3.1 Comparison of the values of U_{opt}^{QE} to calculations

The formalism of the nuclear optical potential of Cooper, Hama, Clark and Mercer [37,38] is phenomenological. They propose a few parametrizations of the optical potential, and determine their dependence on the kinetic energy of the nucleon and radial coordinate by fitting the scattering solutions to the proton-nucleus data for the elastic cross sections, analyzing powers, and spin rotation functions for proton scattering on different nuclei. Since electron and neutrino interactions can occur at any location in the nucleus, it is the average value of the optical potential U_{opt}^{QE} over the entire nucleus that is the parameter that is needed for MC simulations.

The solid blue lines in Figures 3, 4, and 5 are the average nuclear optical potential for final state nucleons U_{opt}^{QE} calculated by Jose Manuel Udias [39] using the formalism of Cooper, Hama, Clark and Mercer published in 1993 [37], and the dashed blue lines are calculated using the later formalism of Cooper, Hama and Clark published in 2009 [38].

As a check, the solid red lines in in Figures 3 and 4 are calculations of U_{opt}^{QE} by Artur. M. Ankowski [40] using Cooper 1993 [37] formalism, and the dashed red lines are calculated using the Cooper 2009 [38] formalism.

The measurements of U_{opt}^{QE} for ^6_3Li and $^{56}_{26}\text{Fe}$ are in good agreement with the Cooper 1993 [37] and Cooper 2009 [38] calculations. The measurements are less negative than the calculations for $^{208}_{82}\text{Pb}$. The measurements are more negative than the calculations for $^{12}_6\text{C} + ^{16}_8\text{O}$, $^{27}_{18}\text{Al}$, and $^{40}_{20}\text{Ca} + ^{40}_{18}\text{Ar}$. For the $^{12}_6\text{C}$ nucleus, although both calculations of U_{opt}^{QE} are above the data, the Cooper 1993 [37] calculations are closer to the data than the Cooper 2009 [38] calculations.

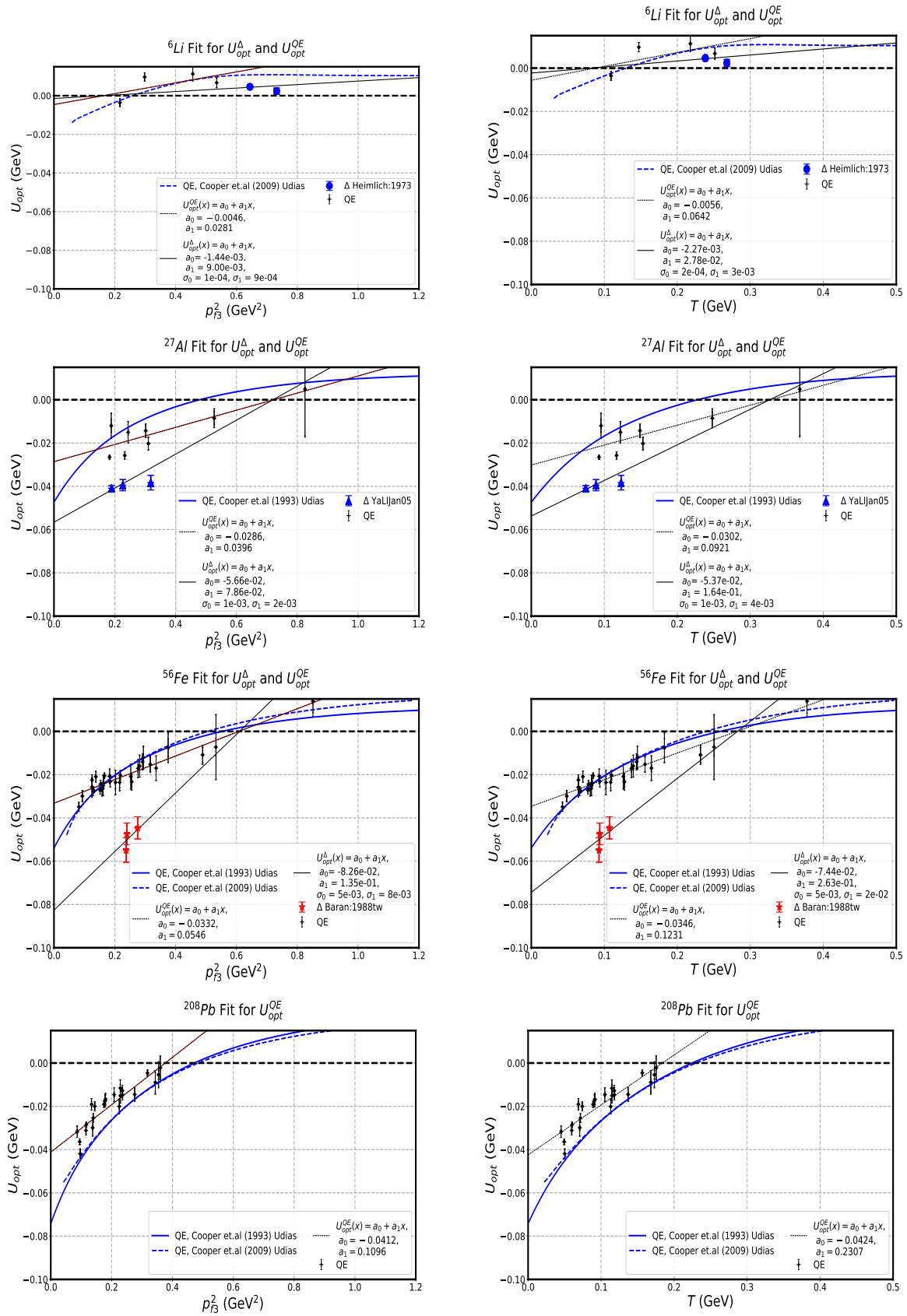


Fig. 5. Same as Fig. 3 for ${}^6\text{Li}$, ${}^{27}\text{Al}$, ${}^{56}\text{Fe}$ and ${}^{208}\text{Pb}$.

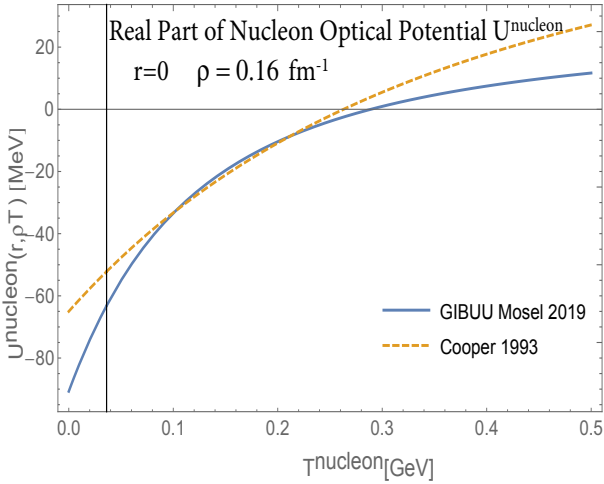


Fig. 6. A comparison of the real part of the nucleon optical potential ($U^{nucleon}(r, \rho, T)$) versus kinetic energy T at $r=0$ and nuclear density $\rho=0.16 \text{ fm}^{-1}$ for GiBUU 2019 [41] as compared to the potential parametrized by Cooper 1993 [37] (curves from Ref. [41]). The two optical potentials are consistent with each other between nucleon kinetic energy between 0.1 and 0.3 GeV^2 (curves from Ref. [41]).

3.2 Discussion of the optical potential for nucleons

We extract the parameter U_{opt}^{QE} which is the average of the real part of the optical potential for the final state nucleon. This parameter is extracted for use in Monte Carlo generators for which the initial state nucleon is described by a spectral function. The spectral function describes the momentum distribution of the nucleon and its removal energy and can be measured in exclusive $ee'P$ electron scattering experiments on nuclear targets. Since the nucleon can be removed from any location in the nucleus, it is the average optical potential that is the relevant parameter. Since we use the measured removal energies to describe the initial state nucleon, the potential which binds the nucleon is not relevant to our analysis.

The GiBUU [41] model describes the initial state as a bound nucleon for which the momentum distribution is related to the local density of nucleons ρ . The nuclear potential $U(\rho, T)$ for the initial state nucleon depends on both the local density and nucleon momentum. The same density and kinetic energy dependent potential is used for the initial and final state nucleons. Figure 6 shows a comparison of the real part of the nucleon optical potential ($U^{nucleon}(r, \rho, T)$) versus kinetic energy T at $r=0$ and nuclear density $\rho=0.16 \text{ fm}^{-1}$ for GiBUU 2019 [41] as compared to the potential parametrized by Cooper 1993 [37] (curves from Ref. [41]). The two optical potentials are consistent with each other for nucleon kinetic energies between 0.1 and 0.3 GeV^2 .

4 Average nuclear optical potential for a Δ resonance in the final state

Several theoretical groups model the quasielastic and Δ production in nuclear targets. The Valencia group [43] uses a local Fermi gas model with RPA correlations. The model accounts for medium effects through the use of nucleon-hole and Δ -hole spectral functions. The Giessen group uses the GiBUU [41,42] implementation of quantum-kinetic transport theory to describe the QE and Δ regions. As mentioned earlier an ingredient in GiBUU is a momentum dependent potential translated into an effective nucleon mass. A summary of various models can be found in reference [44].

The top two panels in Fig. 7 show diagrams for electron scattering from a bound proton producing an invariant mass W in the region of the Δ^+ (left), and scattering from a bound neutron producing an invariant mass W in the region of the Δ^0 (right). The bottom two panels show neutrino scattering from a bound neutron producing an invariant mass W in the region of the Δ^+ (left) and antineutrino scattering on a bound neutron producing an invariant mass W in the region of the Δ^- (right).

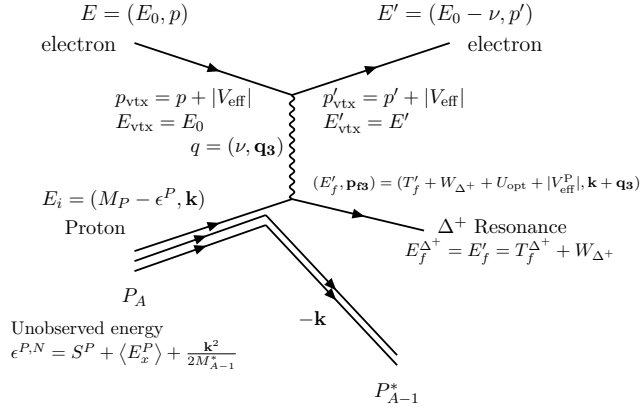
For electron scattering from a bound nucleon the average optical potentials for QE electron scattering and the production of an invariant mass W in the region of the Δ resonance are defined as follows:

$$\begin{aligned}
 \nu + (M_{P,N} - \epsilon^{P,N}) &= E_f & (4) \\
 E_f^P &= \sqrt{(\mathbf{k} + \mathbf{q}_3)^2 + M_P^2} + U_{opt}^{QE} + |V_{eff}^P| \\
 E_f^N &= \sqrt{(\mathbf{k} + \mathbf{q}_3)^2 + M_N^2} + U_{opt}^{QE} \\
 T^{P,N} &= E_f^{P,N} - M_{P,N} \\
 E_f^{\Delta^+} &= \sqrt{(\mathbf{k} + \mathbf{q}_3)^2 + W_{\Delta^+}^2} + U_{opt}^{\Delta} + |V_{eff}^{\Delta^+}| \\
 E_f^{\Delta^0} &= \sqrt{(\mathbf{k} + \mathbf{q}_3)^2 + W_{\Delta^0}^2} + U_{opt}^{\Delta} \\
 T^{\Delta(+,0)} &= E_f^{\Delta(+,0)} - W_{\Delta(+,0)},
 \end{aligned}$$

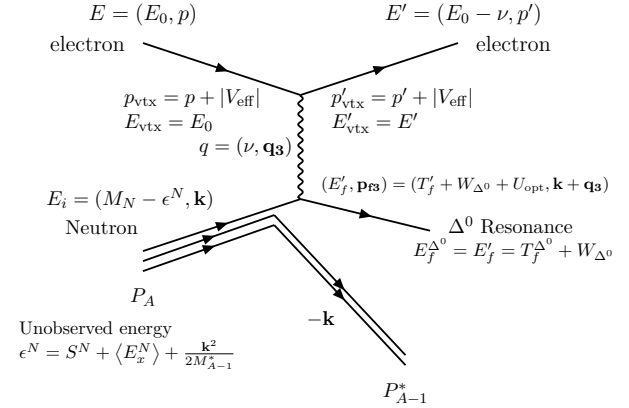
where $W_{\Delta+,0}$ is the final state invariant mass in the region of the Δ resonance and $|V_{eff}^{\Delta^+}| = |V_{eff}^P| = \frac{Z-1}{Z}|V_{eff}|$. Here $T^{\Delta(+,0)}$ is the kinetic energy of the resonance of mass $W_{\Delta(+,0)}$ after it leaves the nucleus and is in the same direction as \mathbf{p}_f .

In order to extract the average nuclear optical potential for a Δ resonance we need to model the cross section between the QE peak and the Δ resonance. We use the effective spectral function [35] (which includes a 2p2h contribution) to model the region of the QE peak. In the calculation of the inelastic cross section for the production of resonances and the continuum we use the Bosted-Christy fits [36] to the inelastic structure functions for free protons and neutrons in the resonance region and continuum. As described in the Appendix, these are fits a wide range of inelastic electron scattering data on protons and deuterons including photoproduction data at $Q^2 = 0$. The fits describe the inelastic structure functions for protons

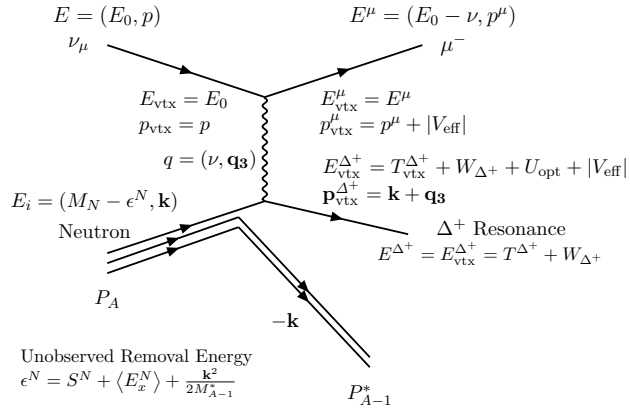
Electron scattering on proton



Electron scattering on neutron



Neutrino Scattering on Neutron



Antineutrino Scattering on Neutron

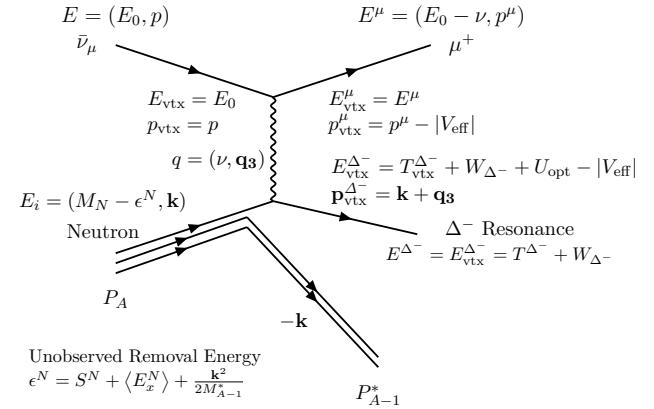


Fig. 7. The top two panels show diagrams for electron scattering from a bound proton producing an invariant mass W in the region of the Δ^+ (left), and scattering from a bound neutron producing an invariant mass W in the region of the Δ^0 (right). The bottom two panels show neutrino scattering from a bound neutron producing an invariant mass W in the region of the Δ^+ (left) and antineutrino scattering on a bound neutron producing an invariant mass W in the region of the Δ^- (right).

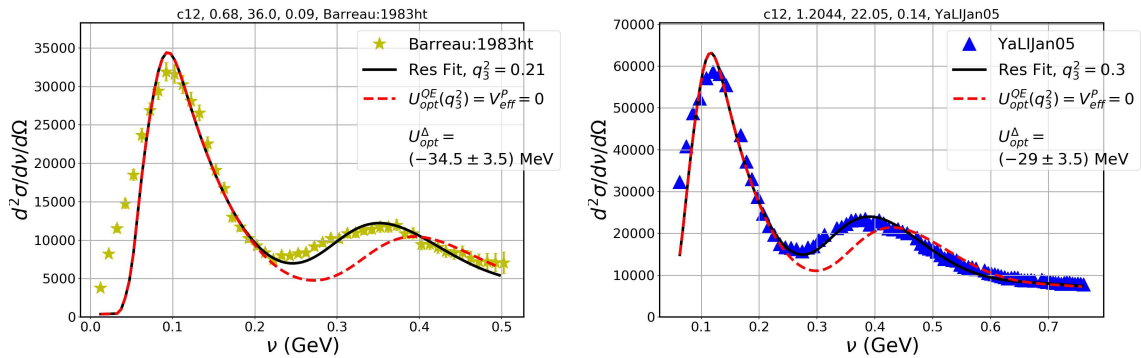


Fig. 8. Examples of fits for two out of 15 ^{12}C $\Delta(1232)$ production differential cross sections. Here the QE peak is modeled with an effective spectral function (including $2p2h$), and Δ production is modeled by using RFG to smear fits to resonance production (and continuum) structure functions on free nucleons. The solid black curves are the fit with the best value of U_{opt}^Δ . The dashed red curves are the predictions with $U_{opt}^\Delta = V_{eff}^\Delta = 0$.

${}^A_Z\text{Nucl}$	$ V_{eff} $ MeV	removal energy ϵ^P, ϵ^N MeV	U_{opt} intercept \mathbf{p}_{f3}^2 $= (\mathbf{q}_3 + \mathbf{k})^2 = 0$	U_{opt} slope vs \mathbf{p}_{f3}^2 $= (\mathbf{q}_3 + \mathbf{k})^2$	U_{opt} intercept $T=0$ GeV	U_{opt} slope vs T GeV/GeV ²
${}^6_3\text{Li}(QE\ proton)$	1.4	18.4, 19.7	-0.005 \pm 0.010	0.028 \pm 0.028	-0.006 \pm 0.011	0.064 \pm 0.057
${}^6_3\text{Li } \Delta^+/\Delta^0 \rightarrow$	± 0.25	(± 3.0)	-0.001 \pm 0.001	0.009 \pm 0.001	-0.002 \pm 0.001	0.028 \pm 0.003
${}^{12}_6\text{C} + {}^{16}_8\text{O}(QE\ proton)*$	3.1	27.5, 30.1	-0.029 \pm 0.004	0.040 \pm 0.010	-0.030 \pm 0.001	0.092 \pm 0.009
${}^{12}_6\text{C } \Delta^+/\Delta^0 \rightarrow$	± 0.25	(± 3.0)	-0.049 \pm 0.001	0.059 \pm 0.001	-0.050 \pm 0.001	0.161 \pm 0.001
${}^{27}_{13}\text{Al}(QE\ proton)$	5.1	30.6, 35.4	-0.029 \pm 0.004	0.040 \pm 0.010	-0.030 \pm 0.004	0.092 \pm 0.023
${}^{27}_{13}\text{Al } \Delta^+/\Delta^0 \rightarrow$	± 0.6	(± 3.0)	-0.059 \pm 0.001	0.079 \pm 0.002	-0.054 \pm 0.001	0.164 \pm 0.004
${}^{40}_{20}\text{Ca} + {}^{40}_{18}\text{Ar}(QE\ proton)*$	7.4/6.3	28.2, 35.9	-0.038 \pm 0.002	0.052 \pm 0.010	-0.038 \pm 0.002	0.110 \pm 0.023
${}^{40}_{20}\text{Ca } \Delta^+/\Delta^0 \rightarrow$	± 0.6	(± 3.0)	-0.059 \pm 0.004	0.083 \pm 0.005	-0.051 \pm 0.003	0.148 \pm 0.009
${}^{56}_{26}\text{Fe}(QE)$	8.9	29.6, 30.6	-0.033 \pm 0.001	0.055 \pm 0.003	-0.035 \pm 0.001	0.123 \pm 0.008
${}^{56}_{26}\text{Fe } \Delta^+/\Delta^0 \rightarrow$	± 0.7	(± 3.0)	-0.083 \pm 0.005	0.135 \pm 0.008	-0.074 \pm 0.005	0.263 \pm 0.020
${}^{208}_{82}\text{Pb}(QE)$	18.9	22.8, 25.0	-0.041 \pm 0.002	0.110 \pm 0.011	-0.042 \pm 0.003	0.231 \pm 0.023
${}^{208}_{82}\text{Pb } \Delta^+/\Delta^0 \rightarrow$	± 1.5	(± 5.0)				
Average all nuclei $\Delta^+/\Delta^0 \rightarrow$			-0.062 \pm 0.001	0.101 \pm 0.002	-	0.284 \pm 0.005

Table 1. The second column shows values of $|V_{eff}|$ (MeV) for various nuclei. The third column shows the removal energies for protons and neutrons (MeV). The 4th and 5th columns show the intercepts (GeV) at $\mathbf{p}_{f3}=0$ and slopes (GeV/GeV²) of linear fits to U_{opt}^{QE} and U_{opt}^Δ versus $\mathbf{p}_{f3}^2 = (\mathbf{q}_3 + \mathbf{k})^2$. The 6th and 7th columns show the results of a similar analysis versus the final state kinetic energy T . The overall systematic error on U_{opt}^{QE} is estimated at ± 0.005 GeV. We show the slopes and intercepts for U_{opt}^{QE} and U_{opt}^Δ on alternate rows. (*The removal energies [6] are (24.1, 27.0) for ${}^{16}_8\text{O}$ and (30.9, 32.3) for ${}^{40}_{18}\text{Ar}$). Note that the fits are only valid in the region for which we have data. Fits for ${}^{12}_6\text{C}$ using a different functional form are give in Table 2.

and neutrons including both resonances and continuum over a wide range of Q^2 .

The Bosted-Christy fits to the proton and neutron structure functions are smeared with a relativistic Fermi gas (RFG) to model the resonance production from nuclei. When comparing to data, the Δ average optical potential is included as a free parameter in the fit. We use a subset of the measured electron scattering cross sections on nuclei that includes measurements of both QE and resonance production. To extract values of the average nuclear optical potential for a $\Delta(1232)$ resonance in the final state (U_{opt}^Δ) we compare the data to predictions of the sum of QE and Fermi smeared resonance production cross sections. In the fits the normalizations of the QE cross section, resonance cross sections and U_{opt}^Δ are varied to fit the data. We only include spectra for which the inelastic continuum is small and the Δ resonance can be clearly identified. We do not include high Q^2 data because the Fermi smearing from the continuum and higher mass resonances is significant and the uncertainty in the determination of the peak of the Δ resonance is much larger.

The systematic error in the extracted value of U_{opt}^Δ is obtained by changing the value of U_{opt}^{QE} by $\pm 50\%$. This shifts the the location of the QE peak relative to the Δ . The best values of U_{opt}^Δ are extracted and the difference in the two extracted values of U_{opt}^Δ is taken as the systematic error.

4.1 Extraction of U_{opt}^Δ from data

Examples of fits for two out of 15 $\Delta(1232)$ production differential cross sections on ${}^{12}_6\text{C}$ are shown in Fig. 8. The solid black curves are the fits with the best value of U_{opt}^Δ . The dashed red curves are the same fits with U_{opt}^Δ and $|V_{eff}^\Delta|$ set to zero. The extracted values of U_{opt}^{QE} and U_{opt}^Δ versus \mathbf{p}_{f3}^2 from 15 ${}^{12}_6\text{C}$ are shown in the top panel of Figure 3. The same values as a function of the Δ kinetic energy T are shown on the bottom panel. The extracted values of U_{opt}^{QE} and U_{opt}^Δ versus \mathbf{p}_{f3}^2 (and T) from 5 ${}^{40}_{20}\text{Ca}$ spectra and one ${}^{40}_{18}\text{Ar}$ spectrum are shown in the top and bottom panels of Fig. 4. Similarly, values extracted of U_{opt}^{QE} and U_{opt}^Δ versus \mathbf{p}_{f3}^2 (and T) for ${}^6_3\text{Li}$, ${}^{27}_{13}\text{Al}$, ${}^{56}_{26}\text{Fe}$. are shown in Fig. 5. For the ${}^{208}_{82}\text{Pb}$ spectra the Fermi smearing is large and we only extract values of U_{opt}^{QE} from the data.

For the ${}^{12}_6\text{C}$ nucleus, the values of U_{opt}^Δ versus \mathbf{p}_{f3}^2 and T^Δ shown in Fig. 3 are fit to linear functions which are shown as solid grey lines. The intercept at $\mathbf{p}_{f3}^2 = 0$ and the slope of the fit to U_{opt}^Δ versus \mathbf{p}_{f3}^2 as well as the intercept and slope of the fit to U_{opt}^Δ as a function of T are also given in Table 1. Fits for ${}^{12}_6\text{C}$ using a different functional form are discussed in the Appendix and shown in Table 2.

As seen in Fig. 3, for the ${}^{12}_6\text{C}$ data, the linear fits to U_{opt}^{QE} and the linear fits to U_{opt}^Δ cross zero at approximately the same values of \mathbf{p}_{f3}^2 (and T). For ${}^{12}_6\text{C}$ we have measurements of U_{opt}^Δ over a sufficient range of \mathbf{p}_{f3}^2 and T to perform a two parameter fit. Because of the small number of measurements of U_{opt}^Δ for all the other nuclei,

we do a one parameter fit for the slopes of U_{opt}^Δ versus \mathbf{p}_{f3}^2 (and T) under the assumption that U_{opt}^Δ crosses zero at the same values of \mathbf{p}_{f3}^2 (and T) as the fits to U_{opt}^{QE} for QE nucleons. The intercepts at $\mathbf{p}_{f3}^2 = 0$ and the slopes of the fits to U_{opt}^Δ versus \mathbf{p}_{f3}^2 (and T) are also given in Table 1. Note that the fits are only valid in the regions for which we have data. We find that $U^\Delta \approx 1.5 U^{nucleon}$ for ${}^{12}\text{C}$.

4.2 Discussion of the optical potential for the the Δ resonance in the final state

4.2.1 Comparison to GiBUU

As mentioned earlier, GiBUU describes the initial state as a nucleon bound in a potential U which depends on both the local density ρ and momentum. The same density and momentum dependent potential is used for the initial and final state nucleon.

For the case of the production of the Δ resonance, the GiBUU formalism requires a density and momentum dependent potential for the Δ resonance in the nucleus. What is used [42] in GiBUU is $U_{GiBUU}^\Delta = (2/3) U_{GiBUU}^{nucleon}$. This is not in agreement with our results which indicate that $U^\Delta \approx 1.5 U^{nucleon}$ for ${}^{12}\text{C}$.

The short lifetime of the Δ (5.63×10^{-24} sec) implies that for the low energy transfers discussed in this paper, the Δ decays occur inside the nucleus. Consequently, one would expect that the optical potential for the Δ should reflect the sum of the corresponding optical potentials of the decay nucleon and pion. This is consistent with our results which show that U^Δ more negative than U^{QE} .

4.2.2 Effective mass of nucleons and Δ resonances in the nuclear medium

Some authors [49] have cast the effect of the nuclear optical potential on the nucleon and $\Delta(1232)$ as an energy dependent change in their effective mass in the nuclear medium. Under this interpretation, both the nucleon and the Δ revert back to their free mass values after leaving the nucleus. For example, the distribution of the final state mass of the decay particles of Δ resonances produced in neutrino-(Propane/Freon) interactions [50] peaks around 1.232 GeV.

At low kinetic energy T , both optical potentials are negative and therefore can be interpreted as a *reduction* in the effective masses of nucleons and Δ resonances when produced in a nuclear medium [49]. Additional details are discussed in the Appendix.

However, as discussed in the next section the effective mass representation is not the appropriate representation for MC generators such as GENIE and NEUT.

4.2.3 Structure functions of bound nucleons

In most impulse approximation Monte Carlo generators, the structure functions of the nucleus are expressed in

terms of a convolution of the nucleon momentum distributions with the structure functions of bound nucleons. The structure functions of bound nucleons are identified with the structure functions of free nucleons expressed in terms of Q^2 and the final state invariant mass W . When the final state invariant mass is the mass of the nucleon, the free nucleon form factors are used. When the mass of the final state is W , the inelastic free nucleon structure functions for the corresponding W and Q^2 are used [46, 47]. Consequently, the interaction of the final state of mass W with the mean field of the nucleus expressed in terms of an average optical potential is more consistent with how the structure functions of bound nucleons are related to structure functions of free nucleons in these Monte Carlo generators,

5 Extraction of neutrino oscillations parameters

5.1 Interaction energy

In the off-shell formalism of Bodek and Ritchie [47], which is used in GENIE, equations 3 and 4 can be written in terms of an energy dependent *interaction energy*:

$$\nu + (M_{P,N} - \epsilon_{QE-interaction}^{off-shell P,N}) = \sqrt{\mathbf{p}_{f3}^2 + M_{P,N}^2} \quad (5)$$

$$\nu + (M_{P,N} - \epsilon_{\Delta-interaction}^{off-shell P,N}) = \sqrt{\mathbf{p}_{f3}^2 + W_{\Delta+0}^2},$$

where

$$\epsilon_{QE-interaction}^{off-shell P,N} = \epsilon^{P,N} + U_{opt}^{QE}(\mathbf{p}_{f3}^2) + |V_{eff}^{P,N}| \quad (6)$$

$$\epsilon_{\Delta-interaction}^{off-shell P,N} = \epsilon^{P,N} + U_{opt}^\Delta(\mathbf{p}_{f3}^2) + |V_{eff}^{\Delta+,0}|.$$

For electron scattering on a nucleon bound in ${}^{12}\text{C}$, our results imply that the *interaction energies* for the range of final state baryon kinetic energies between 0.05 and 0.3 GeV vary from 5 to 28 MeV for the nucleon and from 11 to 29 MeV for the Δ .

In the on-shell formalism of Moniz et al. [45] (used in NEUT) the *Moniz interaction energies* are defined as:

$$\nu + (M_{P,N} + T_i^{P,N} - \epsilon_{QE-interaction}^{Moniz P,N}) = \sqrt{\mathbf{p}_{f3}^2 + M_{P,N}^2}$$

$$\nu + (M_{P,N}) + T_i^{P,N} - \epsilon_{\Delta-interaction}^{Moniz P,N} = \sqrt{\mathbf{p}_{f3}^2 + W_{\Delta+0}^2},$$

where $T_i^{P,N}$ is the kinetic energy of the initial state nucleon (which on average is equal to $\frac{3}{5} \frac{K_F^{P,N}}{2M_{P,N}}$ for a Fermi gas with Fermi momentum $K_F^{P,N}$).

Comparing to Equation 3 we obtain

$$\epsilon_{QE-interaction}^{Moniz P,N} = \epsilon^{P,N} + T_i^{P,N} + U_{opt}^{QE}(\mathbf{p}_{f3}^2) + |V_{eff}^{P,N}|$$

$$\epsilon_{\Delta-interaction}^{Moniz P,N} = \epsilon^{P,N} + T_i^{P,N} + U_{opt}^\Delta(\mathbf{p}_{f3}^2) + |V_{eff}^{\Delta+,0}|.$$

For electron scattering on a nucleon bound in ${}^{12}\text{C}$, our results imply that the *Moniz interaction energies* for the

range of final state baryon kinetic energies between 0.05 and 0.3 GeV vary from 21 to 44 MeV for the nucleon and from 4 to 44 MeV for the Δ .

However, in the analysis of Moniz et al. [45] the *interaction energies* $\epsilon_{QE\text{-interaction}}^{Moniz\ P,N}$ and $\epsilon_{\Delta\text{-interaction}}^{Moniz\ P,N}$ are assumed to be the same which we find is not correct. In addition, the two interaction energies as defined by Moniz are assumed to be constant, which we also find is not correct (these interaction energies depend on both the initial state kinetic energy and on U_{opt} which is a function of kinetic energy of the final state baryon).

5.2 Reducing systematic error in the measurements of neutrino oscillations parameters

As shown above, the *interactions energies* for the nucleon and the Δ are different and over the range of final state baryon kinetic energies from 0.05 to 0.3 GeV they change by about 20 MeV. Using our determinations of the removal energies and energy dependent optical potentials reduces the systematic error in the *interaction energies* for QE-like events from ± 20 MeV to ± 5 MeV.

In reference [6] we estimate that a +20 MeV change in the interaction energy used in the MC corresponds to a change in Δm_{32}^2 of $+0.03 \times 10^{-3}$ eV², which is the *largest* contribution to the total systematic error in Δm_{32}^2 . This estimate is consistent with the estimate of the T2K collaboration which reports [51] that “for the statistics of the 2018 data set, a shift of 20 MeV in the binding energy parameter introduces a bias of 20% for $\sin^2 \theta_{23}$ and 40% for Δm_{32}^2 with respect to the size of the systematics errors, assuming maximal $\sin^2 \theta_{23}$ ”. Consequently in neutrino oscillations experiments our measurements can reduce the systematic uncertainty in the reconstruction of the neutrino energy primarily in experiments such as T2K and Hyper-K [3] that infer the energy of the neutrino from the kinematics of the final state lepton.

6 Conclusions

We report on the extraction (from electron scattering data) of the average nuclear optical potentials for both nucleons and $\Delta(1232)$ resonances in the final state as a function of kinetic energy of the final state baryons. The data show that:

1. *Nucleons optical potential:* The measurements of the average optical potential for a final state nucleon U_{opt}^{QE} for ${}^6_3\text{Li}$ and ${}^{56}_{26}\text{Fe}$ are in good agreement with calculations based on the Cooper 1993 [37] and Cooper 2009 [38] formalisms. The measurements are more negative than the calculations for ${}^{12}_6\text{C}+{}^{16}_8\text{O}$, ${}^{27}_{18}\text{Al}$, and ${}^{40}_{20}\text{Ca}+{}^{40}_{18}\text{Ar}$, and the measurements are less negative than the calculations for ${}^{208}_{82}\text{Pb}$. For the ${}^{12}_6\text{C}$ nucleus, although both Cooper calculations of U_{opt}^{QE} are above the data, the Cooper 1993 [37] calculations are closer to the data than the Cooper 2009 [38] calculations. We

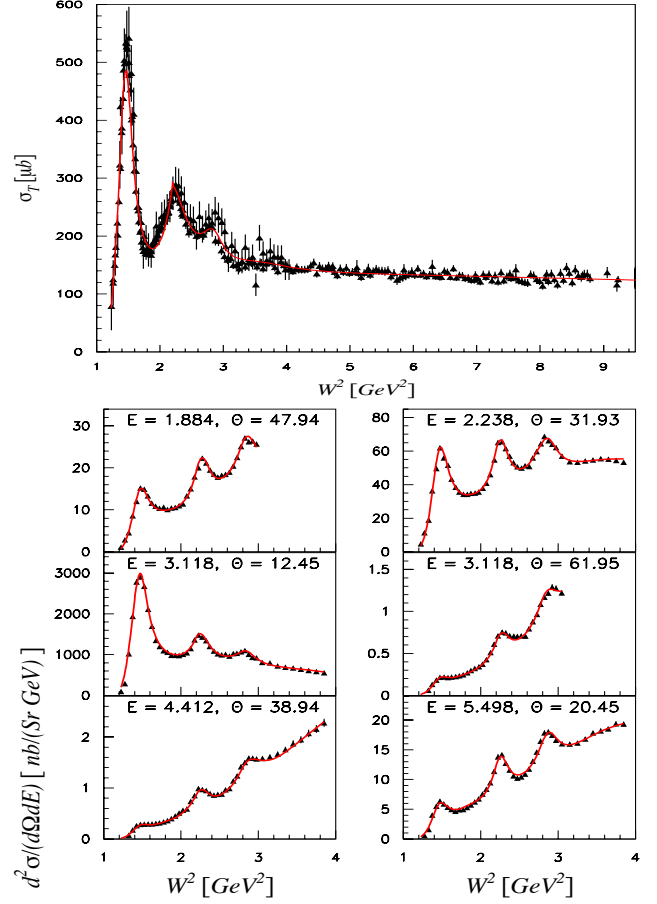


Fig. 9. Examples of Bosted-Christy fits to photoproduction data on protons and Jefferson lab electron-proton cross sections in the resonance region. Curves are from reference [36].

provide fits to the nucleon optical potentials for use in modeling of QE neutrino scattering on nuclear targets.

2. *Δ optical potential:* We find that the average optical potential for a Δ resonance in the final state U_{opt}^{Δ} is more negative than the average optical potential for a final state nucleon with $U_{opt}^{\Delta} \approx 1.5 U_{opt}^{QE}$ for ${}^{12}_6\text{C}$. This is different from the optical potential used in GiBUU [42] for which $U_{GiBUU}^{\Delta} = (2/3) U_{GiBUU}^{nucleon}$ is assumed. We provide fits to the nucleon optical potentials for use in modeling Δ resonance production in neutrino scattering on nuclear targets.
3. *Modeling QE-like events:* Using the measurements of these four parameters $\epsilon^{P,N}$, U_{opt}^{QE} , U_{opt}^{Δ} , and V_{eff} we can model the energies of leptons, nucleons and Δ resonances in the final state for QE-like events. For neutrino oscillations experiments these measurements can reduce the systematic uncertainty in the reconstruction of the neutrino energy primarily in experiments such as T2K and Hyper-K [3] that infer the energy of the neutrino from the kinematics of the final state lepton.

7 Appendix

7.1 Bosted-Christy fits to nucleon inelastic structure functions

In the calculation of the inelastic cross section for the production of resonances including the continuum we use the Bosted-Christy fits [36] to the inelastic structure functions for protons and neutrons. These are fits to a wide range of inelastic electron scattering data on protons and deuterons including photo-production data at $Q^2=0$. The fits describe the inelastic structure functions for protons and neutrons including resonances and continuum over a wide range of Q^2 . A comparison of Bosted-Christy fits [36] to photo-production data on protons and to a few examples of electron-proton cross sections measured at Jefferson Lab are shown in Figure 7.1.

The width of the Δ produced in photo-production [52] on free nucleons as well as at very low Q^2 electron scattering on free nucleons is smaller than at larger values of Q^2 . This leads to an *apparent* reduction of the location of the Δ peak in W from 1.232 GeV to ≈ 1.220 GeV at very low Q^2 . This change in the width (but keeping the mass of the Δ at 1.232 GeV) is taken into account in Bosted-Christy fits [36] that we use to parametrize the electro production of resonances on free nucleons. Our analysis also includes the effects of Fermi motion on both the peak location and width of the Δ when produced in the nucleus.

7.2 The effective mass of the nucleon and $\Delta(1232)$ in the nuclear medium

For purpose of comparison to other publications, we transform our results for the average optical potential for the Δ to an equivalent change of the effective mass of the Δ in the nucleus using the following expression with $M_{\Delta}^{free} = 1.232$ GeV.

$$\sqrt{(\mathbf{k} + \mathbf{q}_3)^2 + (M_{\Delta}^{nuclear-medium})^2} = \sqrt{(\mathbf{k} + \mathbf{q}_3)^2 + (M_{\Delta}^{free})^2} + U_{opt}^{\Delta} + |V_{eff}|. \quad (7)$$

Similarly, the peak in the inclusive distribution in W $M_{\Delta}^{centroid-inclusive}$ (but not including the effect of Fermi motion) can be extracted from the following expression

$$\sqrt{(\mathbf{k} + \mathbf{q}_3)^2 + (M_{\Delta}^{centroid-inclusive})^2} = \sqrt{(\mathbf{k} + \mathbf{q}_3)^2 + (M_{\Delta}^{free})^2} + U_{opt}^{\Delta} + |V_{eff}| + \epsilon. \quad (8)$$

In the above expressions we use the average ϵ and $|V_{eff}|$ for neutrons and protons. In order to compare to the analysis of Sealock et.al [17] we show the data for all nuclei on a single plot in Figure 10.

The top left panel of Fig. 10 shows values of U_{opt}^{Δ} versus kinetic energy of the Δ resonance in the final state (for all nuclei). The points can be approximated by the following expression

$$U_{opt}^{\Delta}(\text{GeV}) \approx (-0.0644 \pm 0.0010) + (0.284 \pm 0.005) T^{\Delta}(\text{GeV}).$$

The top right panel shows U_{opt}^{Δ} as $M_{\Delta}^{nuclear-medium}$, the average Δ effective mass inside the nucleus, versus the kinetic energy of the Δ (for all nuclei). The points can be approximated by the following expression

$$M_{\Delta}^{nuclear-medium}(\text{GeV}) \approx (1.166 \pm 0.001) + (0.299 \pm 0.006) T^{\Delta}(\text{GeV}).$$

The bottom left panel shows the centroids of the peak in invariant mass W for the inclusive electron scattering in the Δ mass region ($M_{\Delta}^{centroid-inclusive}$) versus Q^2 (for all nuclei). The points can be approximated by the expression

$$M_{\Delta}^{centroid-inclusive} \approx (1.220 \pm 0.001) + (0.130 \pm 0.03) Q^2(\text{GeV}^2).$$

The bottom right panel shows $M_{\Delta}^{centroid-inclusive}$ versus Q^2 for various nuclei from the paper by Sealock et.al [17]. Here, the Bates points are from O'Connell et.al. [24], and the Saclay points are from Barreau et.al. [16].

Note that unlike our analysis, the $M_{\Delta}^{centroid-inclusive}$ values extracted by Sealock et.al. do not correct for the apparent shift in the centroid from the known decrease of the width of the Δ at low Q^2 (which shift the apparent centroid to lower mass), nor do they correct for the effect of Fermi motion. In addition, the Sealock et.al [17] analysis includes spectra which have a much larger contribution from the continuum than the spectra used in our analysis.

We conclude that the change in $M_{\Delta}^{centroid-inclusive}$ versus Q^2 originates primarily from the dependence of the average optical potential U_{opt}^{Δ} on the kinetic energy of the Δ resonance in the final state.

7.3 Comparison to the analysis of O'Connell and Sealock

A previous extraction of the average nucleon and Δ potentials from electron scattering cross sections on ${}^{12}_6\text{C}$ was published by O'Connell and Sealock [48] in 1990. They find that the potential for the Δ is more negative than the potential for the nucleon with $U^{\Delta} \approx 2.5 U^{nucleon}$ for ${}^{12}_6\text{C}$. Although qualitatively their conclusions are similar to ours, there are significant differences between the two analyses

As shown in the top panel of Fig. 11 the spectra used in the analysis of O'Connell and Sealock have much larger contributions from the continuum than the spectra used in our analysis. Consequently, we believe that their results for the average potential for the Δ resonance should have an additional model uncertainty. Nonetheless, comparisons between their results and our results for the optical potentials for the nucleon and the Δ are discussed below,

In the O'Connell and Sealock analysis the nucleon optical potential is used for both the initial state and final state nucleons. A specific functional form is assumed for both the nucleon and Δ nuclear potentials. Equations 2

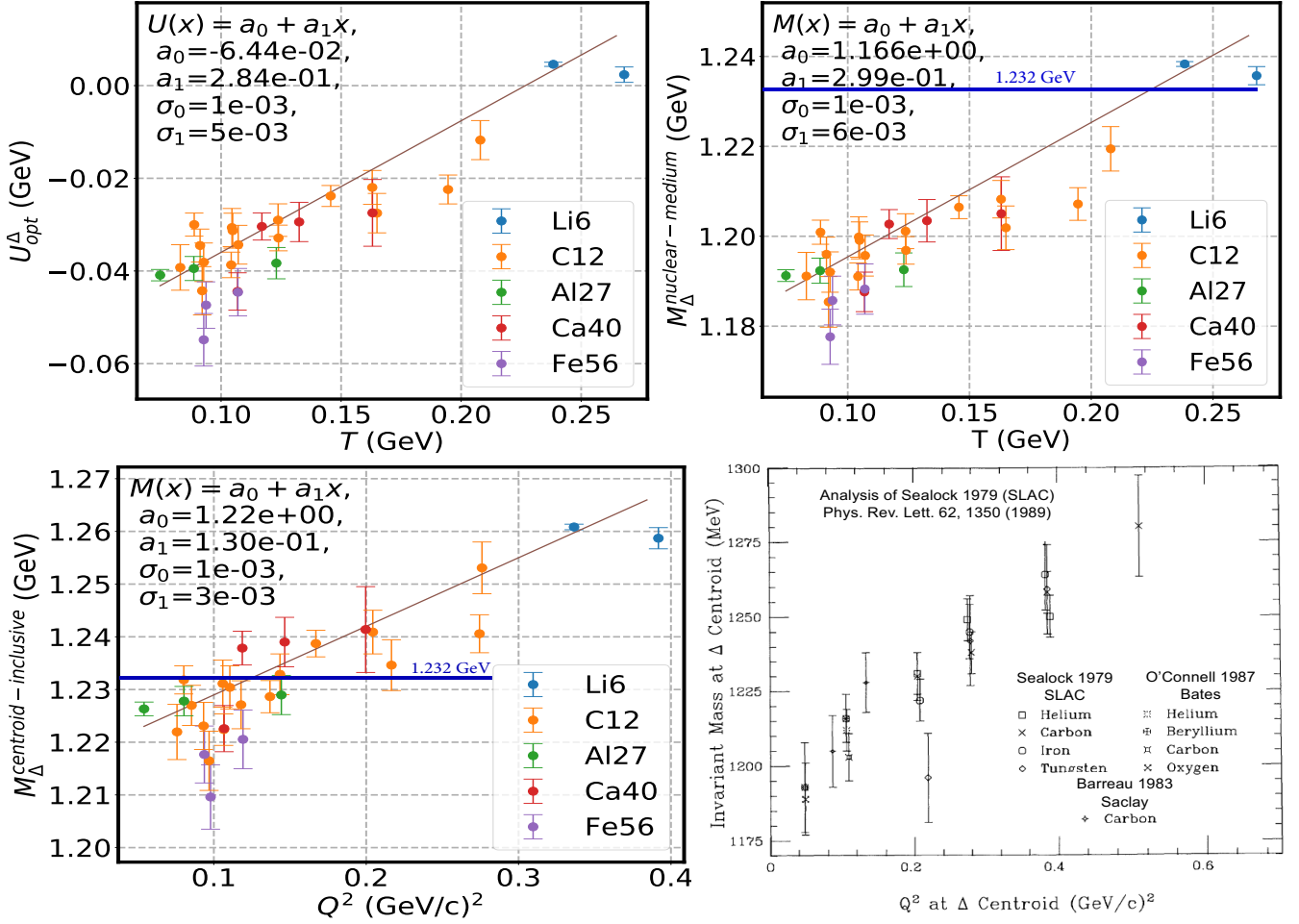


Fig. 10. (a) The top left panel shows values of U_{opt}^{Δ} versus kinetic energy of the Δ resonance in the final state (for all nuclei). (b) The top right panel shows values of $M_{\Delta}^{nuclear-medium}$, the effective average Δ mass while inside the nucleus, versus the kinetic energy of the Δ (for all nuclei). (c) The bottom left panel shows values of $M_{\Delta}^{centroid-inclusive}$ (the centroid of the peak in invariant mass W for the inclusive electron scattering in the Δ mass region) shown versus Q^2 (for all nuclei). (d) The bottom right panel shows values of $M_{\Delta}^{centroid-inclusive}$ versus Q^2 for various nuclei from the paper by Sealock et.al [17]. Here, the Bates points are from O'Connell et al. [24], and the Saclay points are from Barreau et al. [16]. Our results indicate that the change in $M_{\Delta}^{centroid-inclusive}$ versus Q^2 originates primarily from the dependence of the average optical potential U_{opt}^{Δ} on the kinetic energy of the Δ resonance in the final state.

and 3 are not used in the O'Connell-Sealock analysis. Instead the following expression for QE scattering is used

$$\nu + \sqrt{(p_i^2 + M_{P,N}^2 + U_{O'Connell}^{nucleon}(p_i^2))} = \sqrt{(\mathbf{k} + \mathbf{q}_3)^2 + M_{P,N}^2 + U_{O'Connell}^{nucleon}(p_f^2)},$$

and the following expression is used for inelastic scattering with a final state invariant mass W .

$$\nu + \sqrt{(p_i^2 + M_{P,N}^2 + U_{O'Connell}^{nucleon}(p_i^2))} = \sqrt{(\mathbf{k} + \mathbf{q}_3)^2 + W^2 + U_{O'Connell}^{\Delta}(p_f^2)},$$

where $p_i^2 = K_F^2/2$. Both nuclear potentials are then fit to the following functional form

$$U = \frac{V_0}{1 + p^2/p_0^2} + V_1. \quad (9)$$

However, since removal energy information is not used in the O'Connell and Sealock analysis, $U^{nucleon}(p_i^2 = K_F^2/2)$ is not constrained by the differential cross sections. Consequently, for the nucleon they set $V_1^{nucleon}$ such that the fit to the nucleon potential yields $U^{nucleon}(p_i^2 = K_F^2/2) = 41$ MeV.

Comparing their expressions to equation 3 we can estimate

$$U^{P,N}(p_i^2) = \epsilon^{P,N} + T_i^{P,N}$$

which yields 40.4 MeV for the proton and 43.0 MeV for the neutron for $p_i^2 = (1/2)K_F^2$ ($T=12.5$ MeV), and 43.0 MeV for the proton and 45.6 MeV for the neutron for $p_i^2 = (3/5)K_F^2$ ($T=15$ MeV), which is the average kinetic energy for a Fermi gas. Therefore, their assumption that $U^{nucleon}(p_i^2 = K_F^2/2) = 41$ MeV is consistent with our values of the removal energies within an uncertainty of 3 MeV.

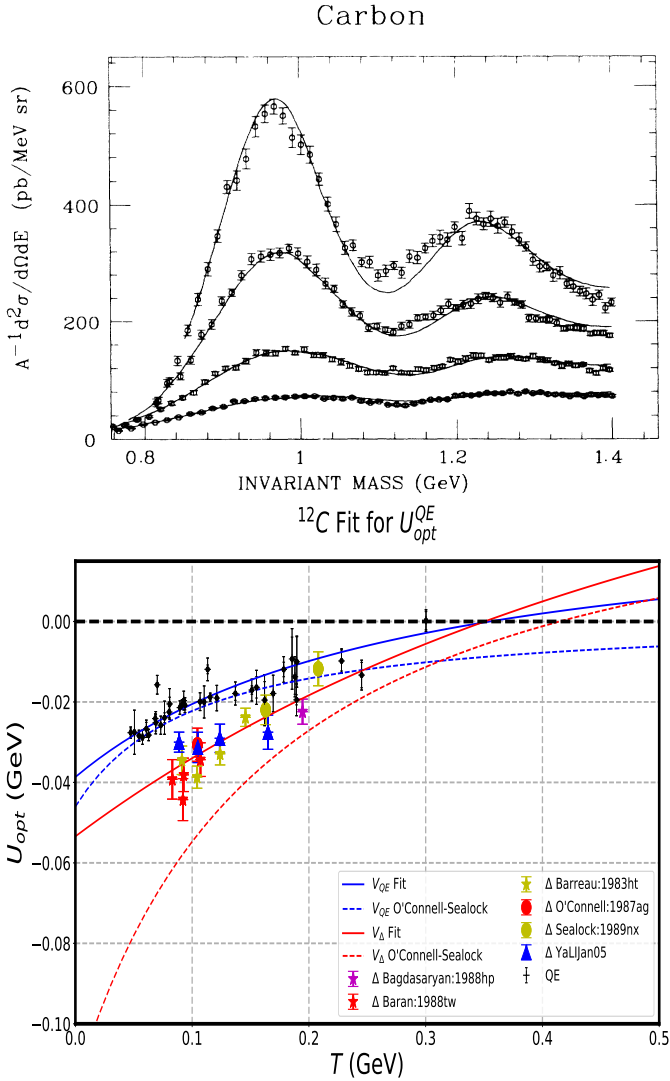


Fig. 11. Top panel: The differential cross sections (as a function of final state invariant mass) used in the O'Connell and Sealock [48] analysis on ^{12}C . All these data were taken at a spectrometer angle of 37.5° . The beam energies from top to bottom are 0.96, 1.1, 1.3 and 1.5 GeV. We note that the contributions from the continuum is much larger than for the cross sections used in our analysis. Bottom panel: Comparison of the O'Connell-Sealock fits for U_{opt}^{QE} and U_{opt}^Δ for ^{12}C to our data. Our fits (using the same functional form $U = V_0/(1 + p^2/p_0^2) + V_1$) are shown as solid lines and the O'Connell-Sealock fits are shown as dashed lines.

Analysis	Final state	V_0 MeV	V_1 MeV	p_0 GeV
This analysis	N	-62 ± 2	23 ± 4	0.691 ± 0.049
	Δ	-138 ± 6	85	1.253 ± 0.117
OConnell+	N	-46 ± 6	0	0.430 ± 0.100
Sealock	Δ	-153 ± 22	38 ± 3	0.628 ± 0.088

Table 2. Comparison of our fits to U_{opt}^{QE} and U_{opt}^Δ for ^{12}C to the O'Connell-Sealock fits using the same functional form $U = V_0/(1 + p^2/p_0^2) + V_1$.

For comparison, we also fit our values for the average optical potentials for the nucleon and Δ to the functional form given in equation 9. For the nucleon, there is sufficient data to extract all of the fit parameters. For the Δ we set $V_1 = 85$ MeV, for which the potentials for the Δ and the nucleon cross zero at the same value of kinetic energy T . Comparison of the O'Connell-Sealock fits for U_{opt}^{QE} and U_{opt}^Δ for ^{12}C to our data are shown in the bottom panel of Fig. 11. Our fits (using the same functional form $U = V_0/(1 + p^2/p_0^2) + V_1$) are shown as solid lines and the O'Connell-Sealock fits are shown as dashed lines.

A comparison of the fit parameters extracted in our analysis, and the parameters from O'Connell and Sealock are given in Table 2. Note that the O'Connell-Sealock fits are only valid in the region of p_f^2 between 0.16 and 1.0 GeV^2 ($0.08 < T^N < 0.43$, $0.06 < T^\Delta < 0.36$). As can be seen in the bottom panel of Fig. 11 the O'Connell-Sealock fit for the average potential for the nucleon is in good agreement with our data.

However, the O'Connell and Sealock fit for the average potential for the Δ is much more negative than our data. And, as mentioned before, the spectra used in the analysis of O'Connell and Sealock (top panel of Fig. 11) have much larger contributions from the continuum than the spectra used in our analysis. Consequently, we believe that their extractions of the average potential for the Δ resonance have additional model uncertainties.

References

1. D.G. Michael *et al.* (MINOS), Phys. Rev. Lett. **97**, 191801 (2006); P. Adamson *et al.* (MINOS), Phys. Rev. D **81**, 072002 (2010).
2. P. Adamson *et al.* (NOVA), Phys. Rev. D **93** 051104 (2016) (<http://www-nova.fnal.gov/>)
3. M. H. Ahn *et al.* (K2K), Phys. Rev. D **74**, 072003 (2006); Y. Ashie *et al.* (SuperK), Phys. Rev. D **71**, 112005 (2005); Y. Itow *et al.* (T2K), arXiv:hep-ex/0106019; The Hyper-K Proto-Collaboration, <https://arxiv.org/abs/1805.04163>.
4. A. A. Aguilar-Arevalo *et al.* (MiniBooNE), Phys. Rev. Lett. **98**, 231801 (2007)
5. The DUNE Collaboration, B. Abi *et al.* "The DUNE Far Detector Interim Design Report Volume 1: Physics, Technology and Strategies" arXiv:1807.10334 [physics.ins-det]
6. Arie Bodek and Tejin Cai, "Removal Energies and Final State Interaction in Lepton Nucleus Scattering" Eur. Phys. J. C **79** (2019) 293. (arXiv:1801.07975 [nucl-th] 2018).
7. P. Gueye *et al.* "Coulomb distortion measurements by comparing electron and positron quasielastic scattering off ^{12}C and ^{208}Pb ", Phys. Rev. C **60**, 044308 (1999).
8. W. Reuter *et al.*, Phys. Rev. C **26**, 806 (1982).
9. C. Andreopoulos [GENIE], Acta Phys. Polon. B **40**, 2461 (2009), C. Andreopoulos, Nucl. Instr. Meth. A **614**, 87, 2010.
10. H. Gallagher (NEUGEN), Nucl. Phys. Proc. Suppl. **112** (2002).
11. Y. Hayato (NEUT), Nucl. Phys. Proc. Suppl. **112**, 171 (2002).
12. "Quasielastic Electron Nucleus Scattering Archive"; O. Benhar, D. Day and I. Sick, Rev. Mod. Phys. **80**, 189-224, 2008

13. O. Benhar, D. Day, I. Sick, “An archive for quasi-elastic electron-nucleus scattering data”, arXiv:nucl-ex/0603032,
14. F. H. Heimlich et al., “High-energy electron scattering from 6Li and 12C”, Nucl. Phys. A231, 509 (1974) (Li6, C12 Heimlich:1974rk).
15. R. R. Whitney et al. Phys. Rev C 9, 2230 (1974) (Li6,C12,Ca40,Pb208 Whitney:1974hr).
16. P. Barreau et al., “Deep-inelastic electron scattering from carbon” Nucl. Phys. 402A, 515 (1983) (Saclay, C12 Barreau:1983ht).
17. R. Sealock et al. “Electroexcitation of the Δ in nuclei”, Phys. Rev. Lett., 62, 1350 (1989) (SLAC, C12, Fe56 Sealock:1989nx).
18. D. Baran et al., Phys. Rev. Lett., 61, 400 (1988) (C12, Fe56 Baran:1988tw).
19. Bagdasaryan, D. S. and others, YERPHI-1077-40-88 (C12, Fe56 Bagdasaryan:1988hp).
20. Diethelm Zeller, DESY Internal Report F23-73/2 (1973); F.H. Heimlich et al. DESY Report 74/20 (1974) (C12 Zeller:1973ge).
21. J. Arrington et al. Phys. Rev C 53 (1996) 2248 (C12, Fe56 Arrington:1995hs).
22. N. Fomin, et al., Phys. Rev. Lett. 105, 212502 (2010) (C12 Fomin:2010ei).
23. M. Anghinolfi et al. (O16 Anghinolfi:1996vm). Nucl. Phys. A602, 405 (1996)
24. J. S. O’Connell et al. “Electromagnetic excitation of the Δ resonance in nuclei”, Phys. Rev. C 35, 1063 (1987) (Bates, C12, O16 O’Connell:1987ag); J. S. O’Connell et al. “Electron Scattering in the Excitation Region of the Delta Resonance on Nuclei with A=1 to 16”, Phys. Rev. Lett. 53, 1627 (1984)
25. H. Dai et al. (The Jefferson Lab Hall A Collaboration), “First measurement of the Ar(e,e’)X cross section at Jefferson Laboratory”, Phys. Rev. C 99, 054608 (2019), arXiv:1810.10575 [nucl-ex]; M. Murphy et al. (The Jefferson Lab Hall A Collaboration), “Measurement of the cross sections for inclusive electron scattering in the E12-14-012 experiment at Jefferson Lab”, Phys. Rev. C 100, 054606 (2019) (Ar40 E12-14-012).
26. M. Anghinolfi et al., “Inclusive electron scattering from an oxygen and argon jet target” J. Phys. G: Nucl. Part. Phys. 21 (1995) L9-LI5. (Ar40 Anghinolfi:1995).
27. P.Y. Bosted et al. Phys. Rev C 46, 2505 (1992) (Al27 Bosted:1992fy), Steve Rock, private comm. (Al27 Rockpc).
28. C.F. Williamson et al. Phys. Rev. C56, 3152 (1997), Phys. Rev. C. 56 (1997) 3152; T.C.Yates et al. Phys. Lett. B 312 (1993) 382, (Ca40 Williamson:1997).
29. A. Hotta et al. Phys. Rev. C30, 87 (1984), (Fe Hotta:1994).
30. Z.E. Meziani et al., Phys. Rev. Lett. 52, 2130 (1984) (Ca40 Fe56 Meziani:1984is).
31. J. Arrington et al., Phys. Rev. Lett. 82, 2056A, 2059 (1999) (Fe56 Arrington:1998ps).
32. J. P. Chen et al., Phys. Rev. Lett. 66, 1283 (1991) (Fe56 Chen:1990kq).
33. D. B. Day, Phys. Rev. C48, 1849 (1993), (C12, Fe, Al27, Au Day:1993md).
34. A. Zghiche et al., Nucl. Phys. A 572, 513 (1994) (Pb208 Zghiche:1993xg).
35. A. Bodek, M. E. Christy, B. Coopersmith, “Effective Spectral Function for Quasielastic Scattering on Nuclei, Eur. Phys. J. C74 (2014) 3091 arXiv:1405.0583 [hep-ph].
36. M.E. Christy and P.B. Bosted, “Empirical Fit to Precision Inclusive Electron-Proton Cross Sections in the Resonance Region”, Phys. Rev. C 81, 055213 (2010); ibid “Empirical fit to inelastic electron-deuteron and electron-neutron resonance region transverse cross section” Phys. Rev. C 77, 065206 (2009); arXiv:0712.3731 (hep-ph),
37. E. D. Cooper, S. Hama, B. C. Clark, and R.L.M. Mercer, “Global Dirac phenomenology for proton-nucleus elastic scattering”, Phys. Rev. C 47, 297 (1993)
38. E. D. Cooper, S. Hama, and B. C. Clark, “Global Dirac optical potential from helium to lead” Phys. Rev. C 80, 034605 (1993)
39. M. V. Ivanov et al., “Global relativistic folding optical potential and the relativistic Green’s function model”, Phys. Rev., C94, 014608 (2016)
40. Artur M. Ankowski, Omar Benhar, and Makoto Sakuda, “Improving the accuracy of neutrino energy reconstruction in charged-current quasielastic scattering off nuclear targets”, Phys. Rev. D 91, 033005 (2015), arXiv:1404.5687 [nucl-th].
41. U. Mosel and L. Gallmeister (GiBUU), “Cross sections for A(e,e’)X reactions. Phys. Rev. C99, 064605 (2019).
42. O. Buss, T. Gaitanos, K. Gallmeister, H. van Hees, M. Kaskulov et. al. (GiBUU), “Transport-theoretical Description of Nuclear Reactions”, Phys. Rep. 512, 1 (2012), arXiv:1106.1344 [hep-ph]; T. Leitner, O. Buss, L. Alvarez-Ruso, U. Mosel, Phys. Rev. C 79 (2009) 034601 arXiv:0812.0587 [nucl-th].
43. A. Gil, J. Nieves, E. Oset, Nuclear Phys. A 627 (1997) 543, arXiv:nucl-th/9711009 [nucl-th]. arXiv:nucl-th/9711009;
44. L. Alvarez-Ruso et al., “NuSTEC White Paper: Status and Challenges of Neutrino-Nucleus Scattering”, Progress in Particle and Nuclear Physics, Volume 100, 2018, Pages 1-68, arXiv:1706.03621 [hep-ph].
45. E. J. Moniz, et al., Phys. Rev. Lett. 26, 445 (1971); E. J. Moniz, Phys. Rev. 184, 1154 (1969); R. R. Whitney et al. Phys. Rev. C9, 2230 (1974); R. A. Smith and E. J. Moniz, Nucl. Phys B43, 605 (1972).
46. A. Bodek, Phys. Rev. D8, 2331 (1974); A. Bodek et. al. Phys.Rev.D20:1471(1979).; A. Bodek, MIT PhD Thesis (1972), MIT-LNS report COO-3069-116.
47. A. Bodek and J. L. Ritchie, ‘Fermi-motion effects in deep-inelastic lepton scattering from nuclear targets’, Phys.Rev. D23, 1070 (1981).
48. J. S. O’Connell and R. M. Sealock, “Phenomenological Δ -nucleus potential from inclusive electron-nucleus scattering data”, Phys. Rev. C 42, 2290 (1990)
49. See talk by Gerald A. Miller “Pion Nucleus Interactions” at the NuSTEC Workshop on Neutrino-Nucleus Pion Production in the Resonance Region, University of Pittsburgh, Oct. 2-5, 2019.
50. N. M. Agababyan, N. Grigoryan, H. Gulkanyan, A. A. Ivanilov, V. A. Korotkov (SKAT), “Study of the $\Delta^{++}(1232)$ inclusive neutrino production on protons and neutrons (Propane/Freon)”, arXiv:1206.4193 [nucl-ex].
51. Simon Bienstock (2018), “Studying the impact of neutrino cross-section mismodelling on the τ 2K oscillation analysis”, in proceeding of NEUTRINO 2018 poster session 35 contribution 173.
52. M. MacCormick et al. (DAPHNE), “Total photoabsorption cross sections for 1H, 2H, and 3He from 200 to 800 MeV” Phys. Rev. C53, 41(1996).